Catalysis Science & Technology

MINIREVIEW

Synthetic Advancements and Catalytic Applications of Nickel Nitride

S. H. Gage[a], B. G. Trewyn[a], C. V. Ciobanu[b], S. Pylypenko[a*], and R. M. Richards[a*]

Transition metal carbides and nitrides have received a large amount of attention in chemistry and materials science due to their interesting properties and potential to substitute precious metal catalysts. Earth-abundant early transition metal carbides and nitrides were the primary focus of many efforts, while late transition metal alterenatives are less explored. This brief review discusses recently published chemical reports that focus on the controlled synthesis of nickel nitride and its composites. The fundamental properties of nickel nitride, such as thermal, structural, and magnetic properties are examined. Furthermore, implementation of nickel nitride materials as catalysts in energy-related applications are thoroughly covered.

1. Introduction

Metal carbides and nitrides first received attention in the scientific community with the discovery of the platinum-like behavior of tungsten carbide reported by Levy and Boudart.[1] Since then, researchers have endeavored to develop these materials as earth-abundant substitutes for expensive precious metals catalysts. However, the majority of studies have been focused on early transition metal carbides and nitrides, their structural, optoelectronic, and magnetic properties,[2, 3] and performance in a variety of catalytic applications,[4, 5] with numerous reviews.[6-9]

Early transition metal carbides and nitrides have also been implemented as support materials for later transition metal catalysts, such as cobalt and nickel nanoparticles. In some cases, these early transition metal carbide and nitride supports have been shown to alter the catalytic properties and selectivity of the active catalysts.[10, 11] However, the study of independent (stand-alone) later transition metal (iron, cobalt, and nickel) carbides and nitrides has been less developed. Within this family of materials, iron carbide/nitride currently dominants the majority of the literature surrounding later transition metal carbides/nitrides.[12] Cobalt-based systems are more toxic, less earth-abundant, and more expensive than nickel-based materials. Therefore, the development of nickel

nitride nanostructures complements current knowledge of iron and cobalt carbide/nitride materials. As a result, nickel nitride (Ni_3N) continues to gain interest as a potential substitute material for precious metals such as ruthenium, rhodium, palladium, and platinum.

Nickel and nickel nitride nanostructures have been explored in a variety of energy applications, including electromagnetic radiation absorbers,[13-15] energy storage devices,[16-19] photovoltaic devices,[20-22] and in the field of catalysis and electrocatalysis,[23-25] including hydrogenation reactions,[26-29] hydrogen and oxygen evolution reactions.[10, 30-33]

Nickel nitride was first synthesized in the 1940's by flowing ammonia over metallic nickel. This material was found to be thermally unstable, as it decomposed in a nitrogen atmosphere at 440 °C.[34] This represented the first evidence that nickel nitride was a thermally metastable material. Later, X-ray diffraction (XRD) was used to determine the hexagonal closed packed (hcp) structure of Ni_3N, and through thermal decomposition of Ni_3N, other phases of nickel nitride were detected, specifically the face-centred cubic (fcc) Ni_4N.[35] Nickel nitride has also demonstrated chemical fragility, with material degradation occurring at 157 °C in a hydrogen atmosphere[36] and a propensity for irreversible oxidative degradation in NO and CO environments at 200 °C.[37]

In more recent years, both physical and chemical approaches have been explored to synthesize nickel nitride. Physical methods include nitrogen ion implantation,[38] plasma-based nitridation,[39, 40] CVD,[41-45] and sputtering techniques.[46-48] Chemical methods have predominantly involved solvothermal processes using highly reactive azides or hydrazine,[49-52] reactions with supercritical ammonia,[53, 54] and ammonolysis of metallic nickel and nickel salt precursors.[10, 55, 56] However, the methods listed above have inherent drawbacks. Either they are limited to thin film technology or involve the use of toxic chemicals and dangerous temperatures and/or pressures.

[a] Colorado School of Mines, Department of Chemistry, Materials Science Program, 1012 14th Street, Golden, CO, USA 80401
[b] Colorado School of Mines, Department of Mechanical Engineering 1610 Illinois Street, Golden, CO, USA 80401
Email: rrichard@mines.edu
Telephone: 303-273-2087
Email:spylypen@mines.edu
Telephone: 303-384-2140
Fax: 303-273-3629

The focus of this brief review is to give a chemist's molecular view of the state-of-the-art of nanostructured nickel nitride. We begin by discussing fundamental properties of nickel nitride, including the thermal, structural, and magnetic properties. We explain how these physical properties make the nanoscale synthesis of nickel nitride extremely challenging. Nevertheless, scientists have found pathways to circumvent the pitfalls of nickel nitride synthesis. These methods, many of which are detailed in this short review, explore recent innovations to control the size and morphology of nickel nitride nanostructures by means of chemical synthesis and implementation of support materials that not only stabilize nickel nitride, but also impart additional beneficial properties. Herein, we detail the broad catalytic applicability of nickel nitride in processes relevant to biomass upgrading, energy storage, and energy conversion.

2. Fundamental Properties of Nickel Nitride

2.1 Thermal and Structural Properties

The bulk phases of nickel and nitrogen are well studied experimentally[57] and theoretically,[58, 59] and the phases shown in Fig. 1 are, with some exceptions, largely accepted. The only pure stable solid phase is the hcp structure: this is the vertically elongated region in Fig. 1, which is surrounded by zones with segregated liquid and hcp phases (high N content or high temperature) and with segregated fcc and hcp phases. Ni_3N is a lower temperature stable phase on the boundary between the pure hcp and the hcp+fcc zones (Fig. 1). Its atomic structure is shown in Fig. 2, and is akin to the known ε phase of Fe_3N. Planes of nickel atoms stack in an ABAB fashion within the unit cell. Nitrogen atoms occupy the octahedral sites of the nickel lattice (Fig. 2) in an ordered fashion, which minimizes the repulsive N-N interactions. Therefore, nickel nitride (Ni_3N) can be regarded as an interstitial metallic compound, with nitrogen atoms located in interstices.[60]

While the consensus is that Ni_3N is a metallic, interstitial nitride, the Ni-N interaction does possess some ionic character. We performed the Mulliken charge analysis after DFT calculations (GGA, PBE) and found that each Ni atom on average loses 0.23 electrons, while each N atom gains 0.7 electrons. This clearly establishes electron transfer from Ni to N, although not nearly as much as it would be required for a pure ionic material in which the N atom receives 3 electrons, in order to complete its outer shell. In summary, while there is a certain ionic character to the Ni-N bond, Ni_3N is considered an interstitial nitride rather ionic nitride.

Other than the most stable phase, there is sufficient evidence[57] that other bulk phases exist in very narrow regions of the phase diagram, specifically, Ni_2N, Ni_4N cubic, Ni_4N tetragonal, NiN_6. First-principles calculations have been conducted to study the various phases of nickel nitride.[61] The computation revealed that all phases of nickel nitride possess positive formation energies, which indicates that these materials are intrinsically less stable than fcc-Ni and the nitrogen molecule. The hcp-Ni_3N possesses the smallest formation energy (+32.9 meV/atom),[53, 62] with the next most stable phase being rhombohedral Ni_3N (+44.0 meV/atom). These
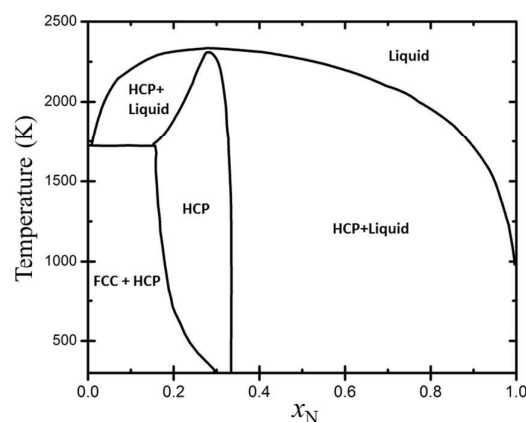

Fig. 1 The Ni-N bulk phase diagram at ambient pressure. Reproduced from ref. 58. Copyright 1991 Plenum Publishing Corporation.

structures differ only in the arrangement of nitrogen in the octahedral sites. In hcp-Ni_3N, the interstitial planes follow ABAB stacking, while in rhombohedral Ni_3N, the interstitial planes have an ABCABC stacking. The difference in formation energy of these two phases is about 11 meV/atom, which is higher than the energy difference between the two most stable phases of nickel carbide. This result validates experimental observations, which indicate that nitrogen disorders less readily than carbon in hcp-Ni structures.[53, 63]

When moving from bulk phases to nanoscale materials and compounds, there are even more reported stoichiometries of nickel nitride, i.e., NiN, Ni_2N, Ni_4N, Ni_8N.[12, 62] The difficulty in synthesizing Ni_3N at the nanoscale lies in the fact that the phase boundaries in Fig. 1 are computed for bulk phases, and they can change for nanoparticles with small radius: thus, even when one plans for the solid phase Ni_3N region in Fig. 1, the synthesis experiments can easily create conditions in which both Ni_3N and fcc nickel are present. Fundamental studies have been conducted to gain better understanding of the structural properties of nickel nitride.[53, 64] In these experiments, Leineweber et al. synthesized nickel nitride using the reaction of hexaamminenickel chloride with sodium amide and degraded in the presence of supercritical ammonia.[53] In a steel autoclave, the reagents were heated to 100 °C and held for 3 hours, before ramping at 30 °C/day to 250 °C. The temperature was then held for 1 week at 250 °C. At this present state, the pressure of the steel autoclave reached approximately 2000 bar. After cooling the vessel to room temperature and releasing the ammonia, the product was washed and dried.

One of the most powerful characterization techniques used in identifying the structure of nickel nitride is X-ray diffraction (XRD). Using XRD (Cu K-alpha source) the hcp structure of Ni_3N is easily discernible from the fcc structure of metallic nickel , as seen in Fig. 3.[40] While this synthetic procedure does yield phase-pure nickel nitride, it is not trivial and has inherent disadvantages. The synthesis involves the formation of a nickel azide intermediate, which is extremely volatile when exposed to air. Furthermore, the long reaction duration is not ideal and handling a steel autoclave at a pressure of 2000 bar can be dangerous.
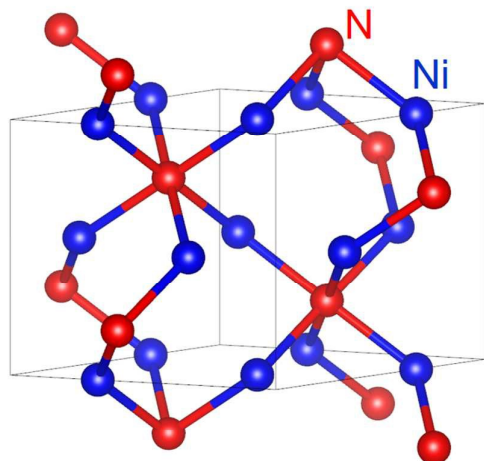
Fig. 2 ε-Fe$_3$N-type structure of Ni$_3$N

For comparison, Leineweber et al. conducted the same experiment without adding liquid ammonia to the vessel.[53] This method formed nickel nitride containing metallic nickel impurities, indicating the vital role supercritical ammonia plays in the experiment. Furthermore, the supercritical reaction state had a tremendous influence on the product morphology. Scanning electron microscopy (SEM) images revealed a more compact structure in the supercritical Ni$_3$N material.[64] It was argued that the increased particle size could be an indication of better molecular transport, due to the ammonia fluid. The authors followed changes in the Ni$_3$N structure as a function of heating conditions, and reported an emergence of a metallic nickel phase starting at 300 °C, which is consistent with previous reports[34, 55, 65] of thermal degradation of nickel nitride at relatively low temperatures. The range of reported degradation temperatures is quite wide, from 287 °C to 440 °C. This indicates that material properties, such as size, shape and purity, may have a profound influence on the thermal stability of nickel nitride.
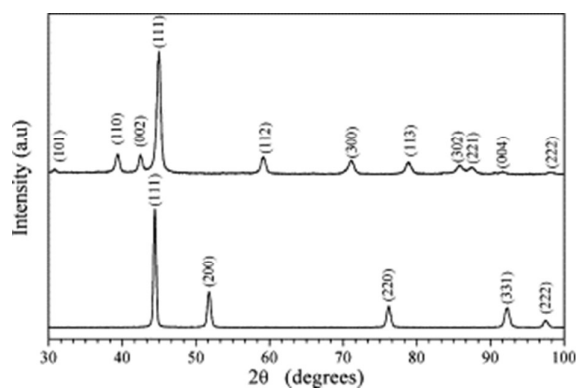

Fig. 3 X-ray diffraction patterns of Ni (down) and Ni$_3$N (up), Reproduced from ref. 40. Copyright 2004 Published by Elsevier B.V.

In a second study, Leineweber et al. grew nickel nitride films on Ni-substrates, in order to explore the material properties at the Ni$_3$N/Ni interface.[64] The experimental results were also correlated to first-principle studies done on the material. Hexagonal Ni$_3$N was grown on pure Ni substrate plates at a range of temperatures (175 °C – 550 °C) under a gaseous nitriding NH$_3$/H$_2$ atmosphere. After the nitridation process, the material was quenched by submersion in water. Cross-sections of the material were examined with XRD and microscopy techniques to reveal a thin Ni$_3$N layer on the Ni-substrate surface.

From the synthesis, the temperature-dependent nitriding potential (r_n) of Ni was found to be much higher than that of other 3d metals. With increasing temperature from 300 °C to 550 °C, the nitriding potential, decreased from approximately 1000 to 100 atm$^{-1/2}$. Nevertheless, this is a few orders of magnitude higher than the nitriding potential of iron under similar conditions.[66] This result is in agreement with the general trend that the thermodynamic stability of 3d transition metal nitrides decreases with increasing atomic number.[67]

The single-crystal elastic constants of Ni$_3$N have been calculated using first-principles density functional theory[64], and indicate a modest degree of elastic anisotropy occurring along the [001] and [uv0] directions. Experimentally, the authors also found that the interface generated by the formation of a nitride layer on the Ni-substrate causes the material to develop an orientation-dependent macrostrain parallel to the surface of the layers.[64] This defect appears to originate during the quenching phase of the synthesis. Upon quenching, a thermal misfit forms between the layers of the materials, due to the different thermal expansion coefficients of Ni$_3$N[53, 63] and Ni.[68]

The authors did report some control over the macrostrains observed in the final product.[64] When the nitridation temperature was increased from 300 °C and 400 °C to 500 °C, a relaxation of elastic strain was observed in the material. This result was corroborated with SEM images, which showed that higher nitridation temperatures lead to higher porosity in the Ni$_3$N layer.

The advantage of this synthetic procedure is the purity of the surface Ni$_3$N layer. Despite an observed elastic strain at the nitride-substrate interface, the lattice parameters in the bulk exhibit little variation, indicating a narrow range of homogeneity in the Ni$_3$N phase. Leineweber et al. did draw comparisons to other chemical routes for Ni$_3$N synthesis.[64] They argued that the nitridation of a nickel substrate forms more pure Ni$_3$N-material, while chemical-based syntheses introduce more heterogeneity in the structural composition. Despite the advantages, this method also has synthetic limitations. Only thin-film Ni$_3$N can by produced, while the bulk of the material remains the Ni-substrate. In addition, this procedure excludes the nano-size regime and generally exhibits limited control over the morphology and size.

2.2 Magnetic Properties

The most recent scientific consensus holds that highly pure nickel nitride is a non-ferromagnetic material,[47, 48] despite some earlier reports that claim nickel nitride is slightly ferromagnetic.[40, 55] The ambiguity of the magnetic and dielectric properties of nickel nitride

in the literature is most likely a result of sample purity. It has been repeatedly demonstrated that nickel nitride has low thermal stability. An introduction of a metallic nickel phase into the nickel nitride structure would thereby introduce a slight ferromagneticity to the non-ferromagnetic nickel nitride. Consequently, the purity of nickel nitride is highly dependent on thermal annealing time and temperature.

The magnetic nature of fcc-Ni vs. hcp-Ni_3N has also been rationalized using first-principles calculations, which indicate that the nonmagnetic phase is most stable for hcp-Ni_3N. This is because, in the case of hcp-Ni_3N, the 3d states of Ni are located close to the valence band. If the material was ferromagnetic, this would facilitate an electron transfer from the nickel 3d states to the nitrogen 2p band. Such a transfer is energetically unfavorable, leading to the non-ferromagnetic phase being of lower energy.

Jia *et al*. recently studied the behaviour of Ni_3N/SiO_2 crystalline nanocomposites under static and dynamic magnetic fields.[15] The Ni_3N/SiO_2 nanocomposite was synthesized by first preparing Ni/SiO_2 by mixing $NiCl_2 \cdot 6H_2O$, N_2H_4 x H_2O (80 wt%), NaOH, ethylene glycol and tetraethyl orthosilicate. The mixture was heated to 70 °C and held at that temperature for 2-4 hours. After being washed and dried, the precursor was calcined in flowing ammonia to yield the final Ni_3N/SiO_2 nanocomposite.

The ammonolysis was performed at both 300 °C and 350 °C for 5-48 hours, in order to determine the influence of nitridation temperature and time on the final product. The TEM inset in Fig. 4 shows Ni/SiO_2 nanoparticles of about 200 nm in size.[15] However after ammonolysis, the nanoparticles do not seem to grow or aggregate, thereby indicating that the immobilization of the nanoparticles onto a SiO_2 support limits Ostwald-ripening and imparts stability to the nanocomposite.

This study reported that ammonolysis of the Ni/SiO_2 at 300 °C for a long duration (48 hours) yielded a fully nitrided product.[15] Furthermore, an increase in temperature to 350 °C for only 5 hours resulted in formation of a fully fcc-Ni phase, due to the decomposition of nickel nitride to nickel and the evolution of nitrogen, according to the following reaction:

$$2\,Ni_3N \rightarrow Ni + 2\,N_2$$
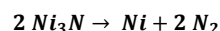
The optimized Ni_3N/SiO_2 material did not exhibit a magnetic response when subjected to both static and dynamic electromagnetic fields, indicating a non-ferromagnetic nature. Interestingly, the Ni/SiO_2 produced by thermally degrading the Ni_3N/SiO_2 nanocomposite at 350 °C exhibited a higher saturation magnetization than the Ni/SiO_2 precursor before ammonolysis. The authors hypothesize that this increase could be due to a cleaner surface, which possesses fewer surface defects due to the thermal annealing under the ammonia atmosphere.[15] This hypothesis, however, was not tested by examining the change in surface roughness as a function ammonolysis duration or temperature.

Later transition metal nitrides have also been studied as potential microwave absorbing materials (MAMs). While this has mostly been limited to iron nitride composites,[69-73] Ni_3N/Ni nanocomposites are now emerging as another MAM candidate, because of the ability to control the magnetic properties of these nanocomposites through
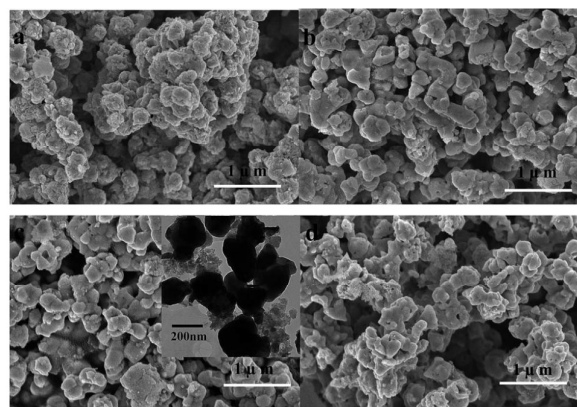

Fig. 4 SEM-images of Ni/SiO_2 (a), 300 °C-12 hr. (b), 300 °C-24 hr. (c), 300 °C-48 hr. (d) The upper right inset shows the corresponding TEM image of 300 °C-24 hr., Reproduced from ref. 15. Copyright 2015 Royal Society of Chemistry

alterations in the material structure. Gong *et al*. recently showed that the thermal decomposition of non-ferromagnetic Ni_3N/SiO_2 introduces the ferromagnetic phase of Ni into the Ni_3N/SiO_2 nanocomposite by evolving nitrogen.[14] This suggests an ability to tune the magnetic properties of metastable metal nitride nanocomposites.

In order to control the "doping" of the Ni_3N/SiO_2 nanocomposite with metallic nickel, the authors calcined the Ni_3N/SiO_2 material in flowing hydrogen/argon mixed gas at different temperatures: 340 °C, 350 °C, and 400 °C for 1 hour to yield $Ni_3N/Ni/SiO_2$ nanocomposites with varying amounts of metallic Ni. In Fig. 5 the emergence of the Ni (200) peak in the XRD (Cu K-alpha source) clearly shows the growth of a ferromagnetic Ni phase through the thermally-controlled decomposition of non-ferromagnetic Ni_3N.[14] Obviously, the mixture of Ni_3N and Ni produces a material with a blending of magnetic properties, which opens the door to new applications. In this particular case, the electromagnetic and microwave absorption properties of this Ni_3N/Ni nanocomposite were studied.

The efficiency of an electromagnetic (EM) wave absorber is dependent on the synergetic relationship between the dielectric loss and magnetic loss of the material. These two properties must be in optimal proportion in a material, in order to induce good EM matching.[74, 75]

While pure Ni_3N is able to dissipate power by dielectric loss, it exhibits poor impedance matching because of its non-ferromagnetic nature. However the growth of a ferromagnetic Ni phase within bulk Ni_3N allows for an adjustment of the balance between dielectric loss and magnetic loss properties. Of all the calcination temperatures, the Ni_3N/Ni composite prepared at 340 °C exhibited the best EM absorption, because it best integrates the magnetic properties of Ni and the dielectric properties of Ni_3N.

This work clearly demonstrates that the thermal decomposition of metastable metal nitrides can be controlled and result in nanocomposite materials with very specific magnetic properties.

3. Hydrogenation Reactions

Catalytically-driven hydrogenation reactions are of vital importance to many industries, including the petrochemical, biomass-conversion, food, and pharma industries. While precious metals such as platinum, palladium, and ruthenium have traditionally exhibited the best overall hydrogenation efficiency, these materials have limited abundance. Since the discovery of Raney-Nickel, nickel-based catalysts have been arguably among the most investigated 3d metals for hydrogenation reactions.[76, 77] Due to its more electron-rich structure, nickel nitride can express unique catalytic selectivity, in contrast to other nickel-based materials.

By now it is well understood that nickel nitride is an interstitial metallic complex whereupon thermal degradation, nitrogen is released from the structure. Thus in the presence of hydrogen, nickel nitride and other metal nitrides may also be of interest as a source of activated nitrogen, which can be further used in reactions with target organic molecules.

In order to test this hypothesis, Alexander *et al*. synthesized nickel nitride by ammonolysis at 480 °C for 6 hours using two different Ni precursors: $NiCl_2$ and NiO.[26] The ammonolysis of $NiCl_2$ to Ni_3N resulted in phase-pure Ni_3N. The same treatment using a NiO precursor did not fully convert the oxide to the nitride, despite the fact that ammonia treated NiO has been reported in the past.[36] This is not overly surprising, as nickel oxide is more thermodynamically stable than Ni_3N.

The authors tested the stability of this material in a hydrogen atmosphere. Not surprisingly, Ni_3N reduced completely at 250 °C in a 1/3 Ar/H_2 flow, with 30 % of the lattice nitrogen converting to ammonia. The remaining 70 % was released as molecular nitrogen. While the authors did not explore different Ar/H_2 gas ratios, it would be interesting to investigate whether gas mixture or flow rate could be altered to maximize the conversion of lattice nitrogen to ammonia.

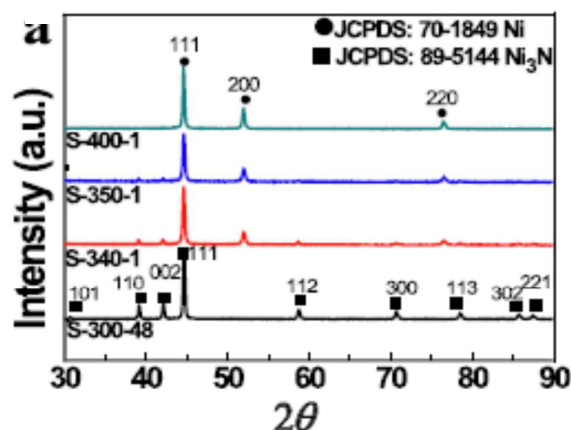This denitridation also resulted in the formation of pores as seen in

Fig. 5 XRD patterns of Ni_3N /SiO_2 composite and Ni_3N / Ni composites obtained under different calcination temperatures: 300 °C, 340 °C, 350 °C, and 400 °C , Reproduced from ref. 14. Copyright 2015 AIP Publishing LLC

SEM images in Fig. 6b, due to the release of sub-surface N_2.[26] However, physisorption measurements were not conducted to determine the influence of the increased porosity on the material surface area. If the change in surface area is substantial, one could use this depletion of nitrogen from Ni_3N to produce high surface area nickel catalysts. This suggests that nickel nitride could potentially be investigated as a dual purpose catalyst, in which reactive nitrogen species interact with target organic molecules and are further catalytically altered in the presence of the remaining porous nickel material.

Molten or eutectic salts are another promising reaction media to produce nanoscale metal nitride materials. By definition when salt components in eutectic salt mixtures are mixed at specific molar ratios, the eutectic salt has a melting point lower than the melting points of the individual salt components in the mixture.[78] Moreover, the use of molten salts has shown to promote the formation of ordered structures and porous materials by acting as a template.[79-81]

Shalom *et al*. recently reported the synthesis of a "sponge-like" Ni_3N-containing material using a $NiCl_2$/LiCl molten salt with a eutectic point of 600 °C.[28] Dicyandiamide (DCDA), which is a common nitrogen source in carbon nitride synthesis,[82] was introduced to the molten salt and thermally degraded under a nitrogen atmosphere to form the Ni_3N-sponge. Transmission electron microscopy (TEM) images show the presence of Ni_3N particles with a broad size distribution, encapsulated in an amorphous nitrogen/carbon matrix. The overall composite is very porous, with a measured surface area of ~350 m^2/g.

When pyrolysis temperatures are elevated to 700 °C and 800 °C, the C/N ratio increases from 1.7 to 3 and 10, respectively. The decrease in nitrogen content is a factor of the degradation of the Ni_3N-sponges to Ni-sponges, as confirmed by XRD analysis. The SEM images in Fig. 7 reveal the porous structure of the Ni_3N- and Ni-sponges, with a visible increase in the porosity, as the pyrolysis temperature is increased from 600 °C to 800 °C.[28]

This also results in a substantial increase in surface area from 350 m^2/g to 580 m^2/g and 906 m^2/g for 700 °C and 800 °C samples, respectively. This can be partially attributed to the evident increase in pore size from ~2 nm in the Ni_3N-sponge to 2.3 nm to 2.5 nm in the Ni-sponges, according to physisorption analysis. The authors rationalize this observation with the understanding that at temperatures above the eutectic point, molten salts disperse more homogeneously throughout the matrix, thereby increasing ultimate
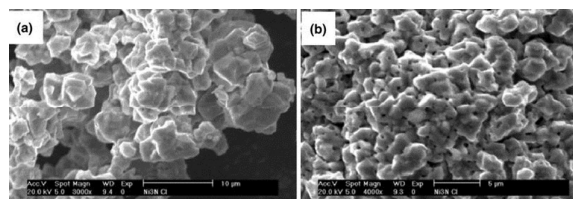

Fig. 6 SEM images of Ni_3N before denitridation at 250 °C (a) and after (b), Reproduced from ref. 26. Copyright 2012 Springer Science+Business Media. LLC

pore size.[80, 83, 84]

This study also found that changing the eutectic point of the salt also changes the temperature at which Ni₃N-sponges can form. The addition of KCl to the mixture lowered the eutectic point to 500 °C, which led to a corresponding decrease in the formation temperature of Ni₃N from 600 °C to 500 °C.[28] Furthermore the additional salt content increases the pore size of the Ni-sponge from 2.5 nm to 3.1 nm in the Ni-sponge pyrolyzed at 800 °C.

The hydrogenation of nitrobenzene to aniline was used as a model reaction to test the catalytic performance of these materials. The results of the hydrogenation of nitrobenzene to aniline[85] comparing samples prepared using different temperatures are shown in Table 1. It is important to note that this reaction had previously only occurred in the presence of catalysts, such as Pd or Pt.[86]

While both Ni₃N- and Ni-sponges demonstrate excellent conversion, the Ni-sponges were superior hydrogenation catalysts, showing good recyclability and oxidation stability. The higher conversion of the Ni-sponge is most likely due to the higher surface area. The authors also report that an increase in the pyrolysis temperature led to a decrease in the carbon and nitrogen content within the final product, which in turn could result in an increase of the surface nickel:carbon ratio. Further investigation using XPS analysis could be used to support this assumption and to confirm the evolution of the surface species, particularly changes in the relative amounts of nickel and carbon-nitrogen species.

Although these Ni- and Ni₃N-sponges are identified as large bulk-like structures by SEM, TEM images did reveal the presence of nanoparticles embedded within the amorphous nitrogen/carbon matrix. The authors, however, only report the existence of a broad particle size distribution in all the samples. A useful follow-up would be to correlate temperature effects on particle size/distribution and the ratio between nickel and the amorphous matrix.

Most importantly, the authors demonstrated that nickel nitride can be synthesized at temperatures much higher than its reported degradation point.[28] The eutectic salt medium appears to impart stability to the nickel precursor. The use of eutectic salt mixtures to synthesize metal nitrides is very promising, because the method does not employ hazardous chemicals and is scalable. Moreover, the tunability of the molten salt medium allows for potentially superior control of the physical and chemical properties of the product. Nevertheless further study on this topic is necessary, in order to synthesize Ni₃N-sponges with a controllable particle size.

The thermal metastability of nickel nitride has been observed repeatedly in the literature. Because of this instability, the synthesis of nano-sized nickel nitride has been elusive. Recently, Clavel et al. synthesized carbon-encapsulated nickel nitride using a low temperature wet chemical, sol-gel type process known as the urea-glass route.[27] The urea glass route involves the formation of metal-urea complexes, which upon thermal degradation under inert atmosphere form metal carbides and nitrides.

The urea-glass route, is a simple and non-toxic method that has shown to create supported nickel nitride/carbide nanoparticles. The enhanced control over particle size and structural composition gives the urea-glass route some benefits over more traditional methods for synthesizing nickel nitride and other transition metal carbides and nitrides.[5, 7, 87]

The thermal degradation of nickel acetate-urea-ethanol complexes in an inert atmosphere results in the formation of nickel nitride nanoparticles, encapsulated within a graphitic carbon matrix.[27] The carbon matrix have two important functions: it acts as a stabilizing media, limiting the aggregation of nanoparticles and also eliminates the need for stabilizing ligands on the particle surface. Both Ni₃N@C and Ni@C were produced by controlling the degradation temperature. As shown in Fig. 8, nickel nitride nanoparticles of ~20 nm were formed at a temperature of 350 °C in a nitrogen atmosphere, whereupon Ni nanoparticles were formed at elevated temperature (450 °C).[27]

The authors performed a suite of hydrogenation model reactions, in order to probe the selectivity of the Ni₃N@C and Ni@C materials.[27] While Ni@C and Ni₃N@C show comparable hydrogenation for nitro groups (>99 %), Ni₃N@C showed poor activity in hydrogenating cyclohexene to cyclohexane (<10 %).

Table 1 Conversion from nitrobenzene to aniline. Reproduced from ref. 28. Copyright 2014 Wiley-VCH Verlag GmbH & Co. KGaA, Weinheimz

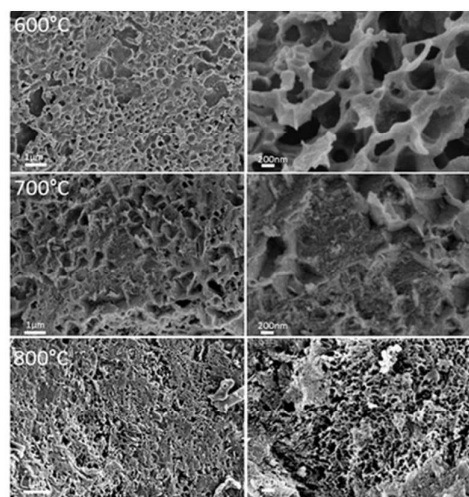| Entry	Sample	Conversion (%)
1	Ni₃N at 600 °C	77
2	Ni at 700 °C	55
3	Ni at 800 °C	>99
4	Ni at 800 °C recycled	98

Fig. 7 SEM images of NiCl₂/LiCl/DDCA materials pyrolyzed at different temperatures. Reproduced from ref. 28. Copyright 2013 Wiley-VCH Verlag GmbH & Co. KGaA, Weinheim

Benzonitrile was also used as a benchmark reagent to test the selectivity of Ni@C and $Ni_3N@C$ catalysts, due to the multitude of possible hydrogenation pathways (Scheme 1). In the comparison to Ni@C, the $Ni_3N@C$ catalyst demonstrated a biselectivity in benzonitrile hydrogenation reactions when subjected to different reaction temperatures. At the lower temperature (55 °C), $Ni_3N@C$ formed dibenzylimine at a >99 % conversion, whereas Ni@C formed mixed dibenzylimine/dibenzylamine products. Furthermore, at higher reaction temperatures (150 °C), $Ni_3N@C$ had an 88 % conversion of benzonitrile to benzylamine, whereas Ni@C continued to fully hydrogenate benzonitrile to dibenzylamine at a 92 % conversion. Under neither the low nor high temperature conditions did the $Ni_3N@C$ material effectively hydrogenate the benzonitrile to dibenzylamine, which gives enhanced synthetic control over product formation.

In addition to having unique temperature-dependant selectivity, the $Ni_3N@C$ material exhibited structural robustness in the presence of pressurized hydrogen. Structural stability test were conducted on the $Ni_3N@C$ material at 25 bar and 75 °C. The XRD diffractogram (Cu K-alpha source) in Fig. 9 demonstrates that even after H_2 treatment, the nickel nitride structure does not degrade to metallic nickel. Furthermore, an elemental analysis of the $Ni_3N@$ material was conducted both after the H_2 treatment and after catalytic test. Table 2 shows that the material does not lose a substantial amount of nitrogen and carbon content after the analyses, which is a demonstration of material robustness.

This work demonstrates that the urea-glass route, which has been so successful in the synthesis of early transition metal carbides and nitrides, can be extended to later 3d metal nitrides. Adjustment of pyrolysis temperature provides additional control over product formation.

Nevertheless, the synthesis of free-standing Ni_3N nanoparticles has not been demonstrated with this method to date. While the carbon matrix provides a high surface area material, the carbon encapsulation could be limiting available active sights on the Ni_3N

Fig. 9 XRD of nickel nitride nanoparticles synthesized at 350°C before and after H_2 treatment (25bar and 75°C). Dotted lines in the XRD diffractogram represent the reference peaks of cubic Ni. Reproduced from Ref. 27. Copyright 2014, Wiley-VCH Verlag GmbH & Co. KGaA, Weinheim

surface. Chemisorption analysis could be paired with physisorption, in order to determine the amount of available metal surface area verses carbon surface area. This would provide valuable insight into the influence of the carbon support on the catalytic properties of the $Ni_3N@C$ nanostructure.

As discussed previously in this minireview, the careful control of pyrolysis temperature can introduce a metallic nickel phase into the nickel nitride structure. This suggests that the construction of $Ni_3N/Ni@C$ nanomaterials with a controlled amount of metallic Ni characteristics may be possible. If properly synthesized these mixed $Ni_3N/Ni@C$ materials could exhibit not only a variety of magnetic properties, but could also potentially possess tuned hydrogenation selectivity to specific functionalities.
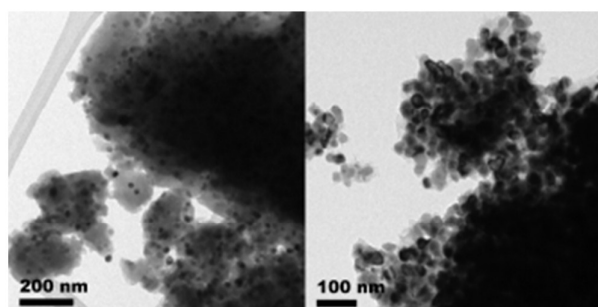

Fig. 8 TEM images of nickel nitride nanoparticles synthesized at 350 °C. (left) and metallic nickel obtained at 450 °C (right). Reproduced from ref. 27. Copyright 2014 Wiley-VCH Verlag GmbH & Co. KGaA, Weinheim
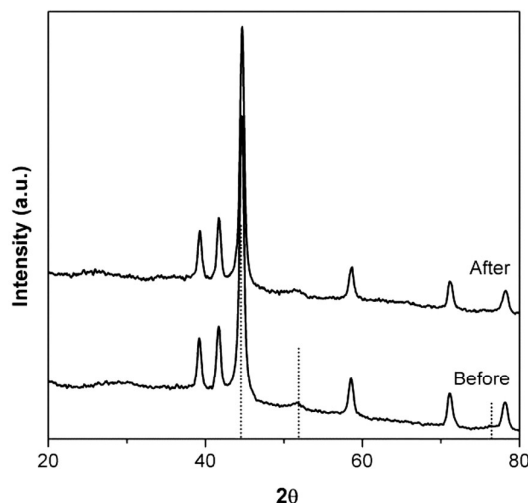
Table 2 Mass% of CHN from elemental analysis of nickel nitride nanoparticles synthesized at 350°C after H_2 treatment and catalytic tests. Reproduced from ref. 27. Copyright 2014 Wiley-VCH Verlag GmbH & Co. KGaA, Weinheim

	N%	C%	H%
Ni_3N 350°C	17.5	16.5	2
After H_2 treatment	15.4	15	2.15
After catalysis	12.75	13.45	1.9

Scheme 1 Reaction mechanism of the formation of benzylamine, dibenzylimine, and dibenzylamine from benzonitrile. Reproduced from ref. 27. Copyright 2014 Wiley-VCH Verlag GmbH & Co. KGaA, Weinheim
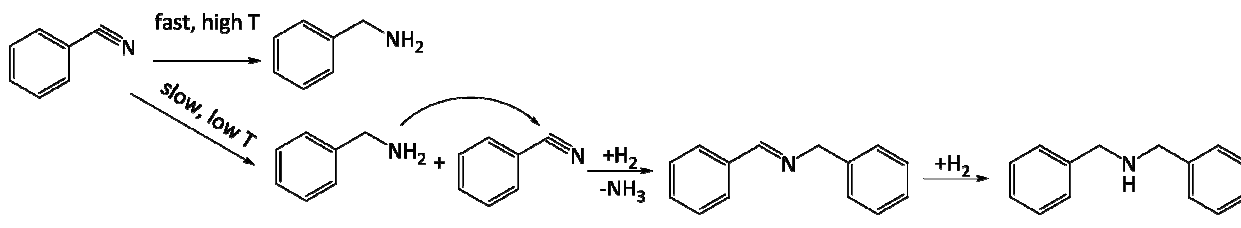
4. Nickel Nitride in Electrocatalysis

The development of low-cost water-splitting catalysts from earth abundant materials is a key component for developing a more sustainable energy production portfolio. Materials with the capability of catalyzing the hydrogen evolution reaction (HER) are key to the efficient production of hydrogen. Meanwhile, the oxygen evolution (OER) and oxygen reduction (ORR) reactions are of particular interest in the development of energy conversion and storage devices, such as fuel cells and metal air batteries. Metal carbides and nitrides have been targeted as a potential replacement for non-earth abundant, noble metal catalysts used in these reactions.[8]

4.1 Hydrogen evolution reaction

Theoretical calculations indicate that metal nitrides may possess electrocatalytic advantages over noble metal catalysts in water-splitting reactions.[10] Most notably, metal nitrides provide higher electrocatalytic activities than their corresponding metallic forms. This increase in the electrocatalytic activity is attributed to higher electron density of the metal nitride surface as compared to pure metal, due to the presence of nitrogen. This results in an increased adsorption of hydrogen to the surface of the metal nitride.[10, 27, 28, 88]

Even so, while metal nitride composites such as Ni–Mo–N or Co–Mo–N have shown particularly high activity as electrocatalysts towards the HER,[88] the most effective electrocatalysts still tend to be precious metals, such as Pt, Ir, and Ru.[88-90] However, recent advances in nickel nitride electrode development are helping to further expand the portfolio of useful alternatives to expensive, precious metal electrocatalysts.

Ni-foams have shown high stability in alkaline solutions and possess low overpotentials and high current density, enhancing the overall conversion efficiency.[91, 92] Recently, Shalom *et al*. produced a Ni_3N/Ni foam material with properties similar to those of Ni-foams.[31] The novel Ni_3N/Ni foams demonstrated low overpotentials (~50 mV) and good stability in alkaline media.

The direct growth of nickel nitride on Ni-foams can be achieved by depositing a cyanuric acid, melamine acid, and barbituric acid (CMB) complex on the surface of a Ni-foam electrode.[31] This nitrogen-rich CMB complex has been shown in the literature to form carbon nitride complexes which, when combined with first row transition metal co-catalysts, create efficient photocatalytic hydrogen producing materials.[93] The authors studied the thermal degradation of this CMB complex on the Ni-foam surface under a nitrogen atmosphere. At 475 °C, the CMB complex degraded to an amorphous carbon-nitride structure, while temperatures between 520 °C and 550 °C pushed product formation to nickel nitride. Further heating of the composite material led to the degradation of the nickel nitride surface layer through loss of nitrogen.

The surface composition chemistry of the Ni/Ni_3N foams was investigated with X-ray photoelectron spectroscopy (XPS). Analysis of the N 1s high resolution spectrum (Fig. 10a) showed that after the heat treatment under nitrogen, nitrogen is present as nickel nitride (398.1 eV) and carbon-nitrogen moieties (398.9 and 399.6 eV) in nitrogen-doped carbon matrix.

Potential cycling of the Ni/Ni_3N material in alkaline solution resulted in evolution of $Ni(OH)_2$ species on its surface. After 500 cycles, the high resolution Ni 2p XPS spectrum (Fig. 9b) confirms the formation of stable $Ni(OH)_2$ on the Ni/Ni_3N material surface.[94, 95] This cycling procedure also removed residual carbon species from the surface. While XPS reveals extensive surface nickel oxidation, XRD characterization shows that the bulk character remains nickel nitride.[31]

In the alkaline HER, the modified $Ni_3N/Ni(OH)_2$ exhibited a 5-fold increase in the electrochemically active surface area as compared to the Ni-foam. The authors hypothesize that this is due to the growth of the hydrous nickel layer on the nitride surface. The presence of a nickel hydroxide layer facilitates the dissociation of water, whereupon protons migrate to the electron rich nickel nitride surface for reduction.[94]

Interestingly, when the $Ni/Ni_3N/Ni(OH)_2$ catalysts were tested in both the OER and HER, the material showed significantly smaller overpotentials and higher current densities in the HER, suggesting that the increased performance is not likely to be attributed to nitrogen-doped carbon. For comparison, the Ni-foams modified with carbon nitride were prepared by thermally treating the precursor material below the formation temperature of nickel nitride. These materials showed lower performance than $Ni/Ni_3N/Ni(OH)_2$ catalysts. It is important to note that temperature plays a very important role in the formation of nitrogen-doped carbons leading to different distribution of nitrogen functionalities. Therefore, it is possible that carbon-nitrogen species formed at lower temperatures might have a different impact on the catalytic activity than those formed at higher temperatures. Nevertheless, the $Ni/Ni_3N/Ni(OH)_2$ catalysts also outperformed these materials.
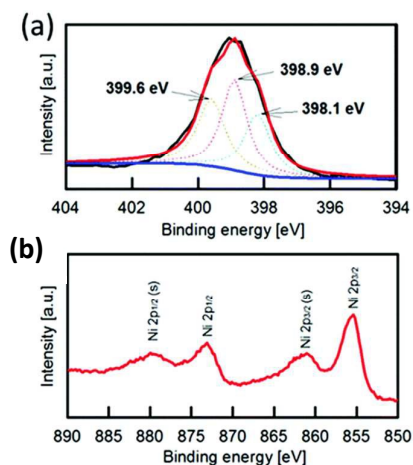
Fig. 10 (a) High-resolution XPS spectra of N 1s; (b) high-resolution XPS spectra of Ni 2p after the carbon-nitride removal (s stands for satellite). Reproduced from ref. 31. Copyright 2015 Royal Society of Chemistry

After 500 oxidation scans, the Ni content in the KOH solution was measured at below 1 ppm, indicating the electrode resists metal leaching. This was further confirmed by XRD analysis, which showed the Ni/Ni$_3$N remained intact after cycling, which reaffirms the robustness of this material.

4.2 Oxygen evolution reaction

While Ni$_3$N/Ni/NiOH$_2$ foams have shown to be effective electrocatalysts in the HER, Ni-based electrocatalysts have suffered in the OER because of low conductivity and poor active site yield. In general, these materials tend to be either semiconducting or insulating, which limits electron transport to the electrode.[96]

A theoretical study of 2-D Ni$_3$N nanosheets, conducted Xu *et al.*, revealed that the density of states (DOS) are located near the Fermi level, which implies that Ni$_3$N is intrinsically metallic.[30] According to the calculations, the carrier concentration and conductivity of Ni$_3$N could be further improved by imposing dimensional confinement. This planar, 2-D confirmation of Ni$_3$N also offers increased contact with the electrode surface and the potential for more disordered structure, which can increase the number of active sites for OER.[10, 96-98]

The authors synthesized the 2-D Ni$_3$N nanosheets by first preparing Ni-nanosheet precursors using a previously published method.[30, 99] In the synthesis, nickel acetate and hexamethylenetetramine were dissolved in water and undergo a hydrothermal treatment at 120 °C for 12 hours. The Ni$_3$N nanosheets were then prepared by heating the Ni-nanosheet precursor at 380 °C (10 °C/min) under a flowing ammonia atmosphere (500 sccm) for 3 hours. For comparison, bulk Ni$_3$N was synthesized by ammonolysis of hexaamminenickel(II) nitrate.[55] On average, the height of the porous Ni$_3$N nanosheet was reported to be 2.15 to 2.95 nm, according to TEM analysis.[30] In addition, temperature-dependent resistivity measurements found that the Ni$_3$N nanosheets had a 3.8 times lower resistivity than that of the bulk Ni$_3$N, which agrees with the first-principle calculations.

The authors conducted extended X-ray absorption fine structure spectroscopy (EXAFS) measurements at the Ni K-edge, in order to

compare the local geometrical structure of Ni$_3$N nanosheets and the bulk Ni$_3$N.[30] The intensity of the Ni-Ni pair decreases in the Ni$_3$N nanosheets to 8.7 from 12 in the bulk Ni$_3$N, which indicates that the nanosheets are a more disordered structure with vacancies resulting from the dimensional reduction.

It is important to highlight that Ni-based catalysts have been investigated for the OER, some of which having a higher OER activity than the Ni$_3$N nanosheets.[100-102] These materials usually achieve good performance by possessing an amorphous structure or being of mixed metallic composition. Thus the activity of the Ni$_3$N nanosheets could be further improved by doping with other elements.

With this in mind, the Ni$_3$N nanosheets were grown on carbon cloth (CC).[30] This hybrid, Ni$_3$N nanosheet/CC nanocomposite exhibited an even higher current density (52.3 mA/cm^2) at lower overpotentials (300 mV) than the unhybridized Ni$_3$N nanosheets, making the material among the most efficient OER catalysts reported in the literature.[103-110] Furthermore as shown in Fig. 11, the Ni$_3$N nanosheets/CC demonstrated a 92 % retention of current density after 18 hours in alkaline solution, which confirms high material stability.[30]

In summary, the 2-D structure of the Ni$_3$N nanosheets ensures better contact with the electrode, thereby improving electron transport within the material. Moreover, the planar configuration contributes to the disordered structure and to the addition of OER active sights within the material. Finally, the implantation of earth-abundant OER electrocatalysts, such as 2-D Ni$_3$N nanosheets, introduces a new regime of materials that could place current state-of-the-art IrO$_2$ and RuO$_2$ electrocatalysts.[111, 112]

5. Energy Storage Devices

Graphene, a monolayer of carbon, has long been used as an anode material for Li-ion batteries due to its many advantages, including high surface area, chemical tolerance, and electrochemical window.[113, 114] Despite its high theoretical Li-storage capacity, all carbon-based electrodes suffer from serious drawbacks, including low initial coulombic efficiency and large capacity fading during
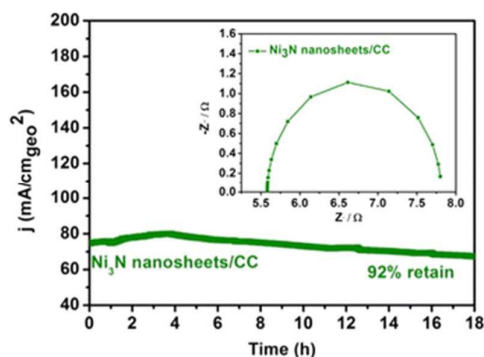

Fig. 11 Chronopotentiometry of Ni$_3$N nanosheets/CC at a overpotential of 0.4 V. Inset: Nyquist plots of Ni$_3$N nanosheets/CC. Note: All the measurements were performed in O$_2$ saturated 1 M KOH solution. Reproduced from ref. 30. Copyright 2015 American Chemical Society

cycling.

While metal oxide-graphene composites have demonstrated high capacitance and longer cycling lifetime than pure graphene,[115, 116] these materials possess a very high discharge voltage. This leads to irreversible reduction of the cell and a decrease in energy density. For this reason, nanostructured transition metal nitrides and nitrides on graphene supports, which demonstrate lower conversion potential and better overall cell stability, have been recently investigated.[117]

5.1 Conversion Reaction with Lithium

The first reported study of the reaction mechanism between nickel nitride and lithium was conducted in 2004 by Wang *et al*.[17] This work had a tremendous influence on the application of the nickel nitride electrode in battery technology, setting the stage for multiple research reports in this area. In this first report, nickel nitride thin-film electrodes were synthesized using reactive pulsed laser ablation on metallic nickel targets in the presence of reactive nitrogen. Nitrogen was activated by applying a DC bias on copper plates positioned between the target and the substrate.

The authors studied the thin film material with XPS, in order to characterize the surface conversion of metallic nickel to nickel nitride.[17] This study represents the first known XPS analysis of nickel nitride. The authors acquired high resolution spectra of both Ni 2p and N 1s and draw conclusions on the chemical composition from the binding energy positions for the peak maxima, without curve-fitting spectra. The N 1s peak maximum was observed at 397 eV, which the authors assigned to be predominantly nitride, due to similarity in peak position for N 1s in Fe_3N.[118] Moreover, the Ni $2p_{3/2}$ peak maximum is observed at binding energies close to those reported for Ni_3P, which the authors believed to further support their hypothesis.[119] The Ni:N ratio was also estimated to be 3.1:1 by integrating the peak areas of the entire Ni 2p and N 1s spectra, respectively. However, without comprehensive fitting of the spectra, which is extremely difficult to do for nickel spectra without appropriate standards, the presence of oxidized nickel species on the surface of the material was not taken into the account. In other words, it is unlikely that 100 % of the surface nickel is chemically associated with nitrogen in the form of nitride. Instead, while the overall Ni:N ratio is 3.1:1, nickel content could be distributed between nitride, oxide, hydroxide, oxyhydroxide species, *etc*.

XPS analysis of the lithiated nickel nitride electrode demonstrated the formation of additional species, such as metallic nickel and Ni^{3+}, which could be either nickel oxyhydroxide species or a higher valency nickel nitride (NiN). Regardless, the reaction of nickel nitride with lithium leads to an irreversible phase conversion of the nickel nitride electrode to metallic nickel, as confirmed by XRD analysis.[17] This conversion was also reportedly visible, as the decrease in the specific capacitance from the 1st to the 2nd cycle is accompanied by a colour change in the material.

Based on their results, the authors proposed the following electrochemical reaction between Ni_3N and Li (1), and the following reversible reduction-oxidation reaction (2):

$$Ni_3N + 3Li \rightarrow 3Ni + Li_3N \qquad (1)$$

$$NiN + 2Ni + 3Li \leftrightarrow 3Ni + Li_3N \qquad (2)$$
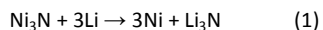
These equations are two potential reaction mechanisms between nickel nitride and lithium, which have served as a blueprint in understanding the lithiation mechanism of nickel nitride.[17] However, the authors could not clearly discern the role of metallic nickel in the reaction mechanisms. In one reaction, metallic nickel is nitrided and reduced in the lithium electrochemical reaction, and another reaction of nickel seems to act as an active spectator to drive the formation and decomposition of Li_3N.

5.2 Ni₃N as Negative Electrode in Lithium-ion Batteries

In order to further probe the electrochemical relationship between nickel nitride and lithium, Gillot *et al*. prepared nickel nitride using three different synthetic routes and electrochemically tested the materials against lithium.[16] The authors investigated the products formed from the thermal treatment of nitrogen-rich nickel salts under a flow of ammonia. This bulk form of nickel nitride was obtained from a commercially available hexaamminenickel(II) bromide ($Ni(NH_3)_6Br_2$) at 500 sccm of ammonia flow at 420 °C for 15 hours.

The particle size of the bulk nickel nitride was approximately 10 μm, with a porous surface structure revealed by SEM.[16] The large pores are believed to form during the thermal decomposition of the precursor, due to the loss of bromine and ammonia.

For comparison, the authors also nitrided preformed 50 nm metallic Ni nanoparticles in a similar thermal ammonolysis reaction. XRD analysis (Cu K-alpha source) in Fig. 12 shows the conversion of Ni nanoparticles to nickel nitride as a function of time of ammonia heat treatment at 260 °C.[16] An ammonolysis duration of 130 hours was required to convert nickel to bulk nickel nitride. In addition, the heat treatment at 260 °C led to particle size growth from approximately 50 nm nickel particles to 1-3 μm sized nickel nitride particles. This further reinforces the challenges in converting a stable metallic nickel to metastable nickel nitride.

For a final comparison, the authors experimented with the thermal decomposition of nickel amide to nickel nitride. This synthesis involved the use of hazardous chemicals, including potassium amide and liquid ammonia. In addition to the hazards, the authors also reported low yields of nickel nitride, due to contaminants, residual nickel amide precursor, or full reduction of the product to metallic nickel. This synthetic route proved to be extremely temperature and time sensitive. Only with a decomposition temperature of 130 °C at a reaction time of about 70 hours was phase pure nickel nitride observed with XRD.[16] Despite these procedural drawbacks, this synthetic procedure produced the smallest nickel nitride nanoparticles, with sizes of approximately 50 nm in diameter as observed by TEM.

The three nickel nitride materials were electrochemically tested against lithium as a potential negative electrode material for lithium ion batteries. Not surprisingly, the nickel nitride nanoparticles prepared with the nickel amide route exhibited the best overall capacity (1200 mAhg^{-1}). This enhanced activity appears to be surface area related, as the nickel nitride materials from the two other synthetic routes had much larger particle sizes. However, the specific capacity quickly declined with increasing number of cycles.
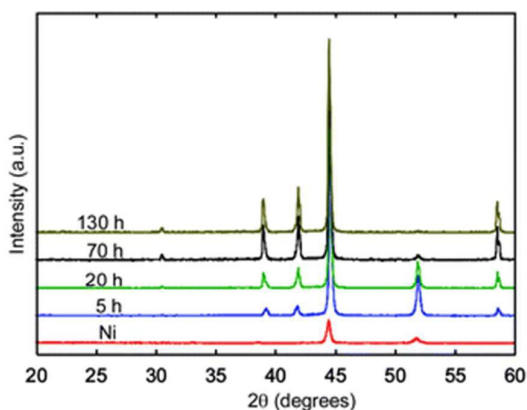
Fig. 12 XRD patterns corresponding to samples prepared through treatment of nickel nanoparticles under ammonia at 260 °C. Reproduced from ref. 16. Copyright 2011 Royal Society of Chemistry
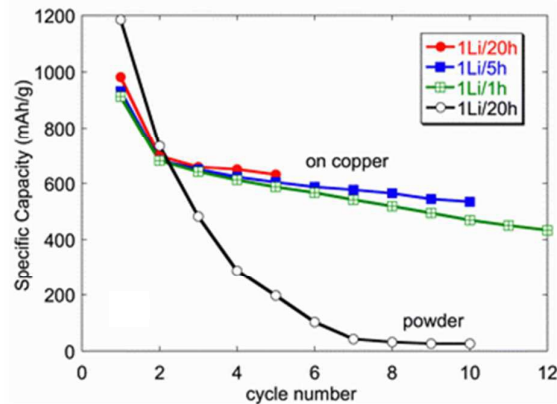

Fig. 13 Capacity vs. cycle number for the same electrodes tested in a galvanostatic mode at different rates. Reproduced from ref. 16. Copyright 2011 Royal Society of Chemistry

In order to maintain capacitance, the best performing nickel nitride material was further improved by casting the nanoparticles on a copper foil electrode. This was done by casting a slurry of sample, carbon black, and binder onto the foil by doctor blading. As seen in Fig. 13, the cast electrodes showed a fairly stable capacity at 500 mAhg^{-1} after 10 cycles at high intensities (1 Li per 5 hours and 1 Li per hour).[16]

The casted nitride electrodes outperformed uncasted nickel nitride nanoparticles, which showed poor reversibility and large capacity fading after the first reduction. More importantly, these results clearly show the necessity to stabilize nickel nitride on a support material. Further studies are required to understand the interactions between nickel and the support material, in order to optimize the performance of this nanocomposite in energy storage devices.

5.3 Ni$_3$N as Negative Electrode in Sodium-ion Batteries

Sodium-based batteries have several advantages over Li-ion batteries. Sodium provides high voltage and similar energy density to lithium. Additionally, sodium is far more abundant and lower in cost than lithium.[120] Although graphite is commonly used as a negative electrode material for Li-ion batteries, graphite cannot intercalate the sodium ion,[121] which necessitates the development of new negative electrodes for sodium-ion batteries.

It has been previously established that metal nitrides can intercalate lithium ions via a conversion reaction mechanism.[16, 17] However, little work has been done to understand the intercalation chemistry of the sodium ion in this system.

For the first time, Li *et al*. recently studied nickel nitride as a negative electrode material in a sodium-ion battery.[18] Nickel nitride was prepared in two manners. First, nickel nitride was synthesized according to a previously reported procedure,[55] by dissolving nickel nitrate hexahydrate in water and adding a 35% solution of NH$_3$ slowly to the nickel nitrate solution. This resulted in a colour change to a bluish-violet solution, signalling the formation of the hexaamminenickel (II) complex. The product was dried by evaporation under flowing NH$_3$ and then further dried in a dessicator over BaO for 3 weeks. Ni$_3$N was prepared by grinding the nickel precursor and heating it under flowing ammonia at 335 °C for 6 hours and 200 °C for 8 hours, respectively.

A second Ni$_3$N material was prepared by reacting anhydrous nickel nitrate with ethylenediamine (EN), creating tris(EN)nickel nitrate. The salt was isolated with vacuum drying and annealed under flowing ammonia at 360 °C for 4 hours and 200 °C for 40 hours, respectively. Ethylenediamine, a bidentating molecule, is a well known complexant in inorganic chemistry. According to the chelate effect, the resulting metal-ethylenediamine complex is more thermodynamically stable than the metal-ammonia complex.[122] Therefore, the thermal degradation of these two nitrogen-containing complex can result in nickel nitride with very different material properties.

The material prepared from the hexaamminenickel (II) precursor was composed of large aggregates as seen in TEM and possessed a surface area of only 2.3 m^2/g, and XRD showed the presence of NiO contamination.[18] Phase-pure Ni$_3$N was only obtained when the product was dried in a dessicator flushed with ammonia. Conversely, a much smaller Ni$_3$N particle size (~20 nm) was synthesized by the ammonolysis of the tris(EN)nickel nitrate precursor. This material also possessed a slightly higher surface area (~16 m^2/g), most likely due to the smaller particle size. However, XRD did reveal that this material also contained a small quantity of metallic nickel, which could not be removed from the final product.[18]

Certainly when degrading large metal organic precursors, the formation of carbon-nitrogen by-products is a real possibility. These by-products could lead to surface contamination and deactivation of the nickel nitride catalyst. The infrared (IR) analysis on the nickel nitride samples (Fig. 14) indicated the presence of organic surface contaminants in the tris(EN)nickel nitrate-Ni$_3$N material, in the form of amine group absorptions at 3150 cm^{-1} (ν(NH)) and 1599 cm^{-1} (δ(NH$_2$)).[123, 124] These absorptions can be attributed to residual

derivatives of ethylenediamine from the thermal degradation of the precursor.

Both Ni_3N materials were tested for their reduction-oxidation behavior vs. sodium foil using 1 M $NaPF_6$ in ethylene carbonate-diethyl carbonate (1 : 1) electrolyte.[125] The first reduction cycle showed an initial capacity of 120 mAhg^{-1} in the hexaammine nickel nitrate-derived Ni_3N and 465 mAhg^{-1} in the tris(EN)nickel nitrate - derived Ni_3N material. In both cases, the capacity fell significantly in the first 5 cycles and stabilized after 30 cycles. The tris(EN)nickel nitrate - derived Ni_3N material possessed the higher specific capacity, which highlights the pivotal role that particle size plays in determining specific capacity.

The specific capacity of Ni_3N after 20 cycles (134 mAhg^{-1}) exceeds the capacity of carbon black with comparable charge and discharge over a similar potential range.[18] With further reduction in nickel nitride particle size, performance of Ni_3N as a negative electrode in sodium-ion batteries can be further improved. Decreasing the particle size will lead to an increase in active surface and thereby an increase in the initial specific capacitance.

However, addressing the particle size issue neither imparts stability to the nickel nitride electrode nor addresses the problem of the sharp decline in electrode performance. A two part solution is necessary, in which small nickel nitride nanoparticles increase the specific capacitance of the electrode and a support material protects the electrode from degradation during cycling.

5.4 Ni_3N on graphene-type supports

In order to address these stability issues, Lai *et al.* recently supported nickel nitride on nitrogen doped reduced graphene oxide nanosheet supports (N-rGO), by annealing metal-ethylenediamine complexes and GO composites.[117] Li-storage and cycling behaviour was tested for three materials prepared with different metals: Fe, Ni, and Co. Even with low metal loading (~12.5 %), the transition metal nitrides (TMN) greatly improved the Li-ion storage capacity of the graphene support.

The GO nanosheets were first synthesized using a modified Hummers method.[126, 127] The NiN/N-rGO was prepared by dissolving
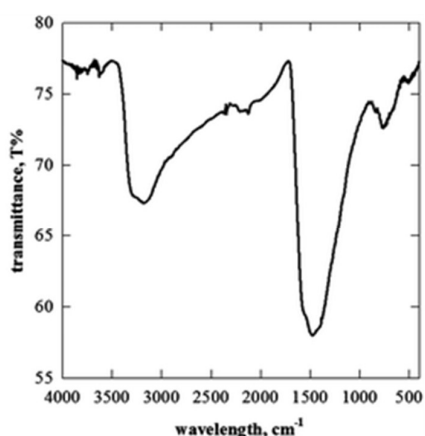
200 mg of nickel nitrate in ethanol and adding 1 mL of EN. The solution was stirred to create the Ni-EN complex. The complexed solution was then added to a 100 mL solution of 2 mg/mL GO and refluxed at 100 °C for an hour at ambient pressure. The precipitate was dried and calcined at 850 °C for 1 hour under NH_3/Ar at a flow rate of 120 sccm. The product was then ground with mortar and pestle and treated with 1 M H_2SO_4 at 80 °C for 12 hours, before being filtered, washed with DI H_2O, and dried under vacuum.

The GO has abundant O-containing functional groups, which are capable of adsorbing TM^{n+}-EN complexes simply through electrostatic interaction. During the reflux step of the synthesis, some O-containing function groups in GO are replaced by $-NH_2$ groups from the TMN^{n+}-EN complex. The synthesis of the TMN/rGO complex can be visualized in the schematic in Fig. 15.[117]

The calcination of the TMN/rGO sample performs three important steps: the formation of TMN nanoparticles, reduction of GO to rGO, and doping of rGO with nitrogen from the EN chelates. TEM analysis confirmed the presence of 1-2 nm sized nickel nitride nanoparticles on the N-rGO surface.[117]

XPS analysis showed that the nitrogen dopants from the EN chelates form covalent C-N bonds with the graphene layers. By fitting the C 1s high resolution spectrum from the TMN-rGO, the authors characterized the carbon species at 284.5 eV, 285.1 eV, and 286.0 eV to be sp^2-hybridized C, C-N bonds, and C-O bonds, respectively. The authors also confirmed the presence of Ni and N by conducting electron energy loss spectroscopy (EELS).[117] The core-loss K-edge of C and N is located at 284 eV and 401 eV, while the L2.3 edge of nickel is present at 850 eV.

The material was tested using cyclic voltammetry against a Li metal counter and a reference electrode. At a current density of 50 mAg^{-1}, the capacity retention of NiN/N-rGO was 730 mAhg^{-1}. Conversely, the reversible capacity of the FeN/N-rGO and CoN/N-rGO was only 698 mAhg^{-1} and 667 mAhg^{-1} after 50 cycles, respectively.

The synthetic approach used in this work yielded very small nickel nitride nanoparticles with increased active surface area. Moreover, the immobilization of the nanoparticles on a reduced graphene oxide nanosheet support imparted stability to the fragile material. The N-doping of the rGO was found to greatly improve graphene

Fig. 14 IR Spectrum of Ni_3N derived from ammonolysis of $[Ni(EN)_3]\cdot 2NO_3$. Reproduced from ref. 18. Copyright 2013 Royal Society of Chemistry

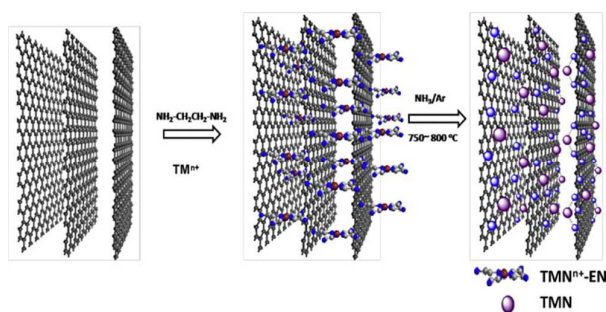**Fig. 15** Schematic illustration for the preparation of TMN/N-rGO. Reproduced from ref. 117. Copyright 2014 Elsevier Ltd.

conductivity, by further enhancing the separation and transportation of ions in the material, thereby leading to improved capacity and cyclability. In all, the system demonstrated not only high initial capacitance, but also stable capacitance through 50 cycles, which is a vast improvement over reports mentioned previously in this minireview. It is important to state that the majority of research on 3d metals in $LiTM_xN_y$ materials has been directed towards Co_3N and Fe_3N.[128] Ni_3N still remains largely unexplored. Nevertheless, the excellent cyclability, low charge/discharge potentials (<1.5 V), high reversible capacity values of Ni/N-rGO indicate that this material could be considered a prospective anode material for Li-ion batteries.

While in general graphene-supported nickel oxide catalysts have been extensively studied as pseudocapacitive materials,[129-134] Yu *et al.* recently investigated nickel nitride nanostructures on rGOs as a potential electrode material for pseudo-supercapacitor devices.[19]

The use of nickel-based electrode materials for pseudo-supercapacitors is challenging for two important reasons. Firstly, pseudo-supercapacitors store energy through a change in faradic charge. Nickel oxides are limited to the faradic redox reaction of only Ni (II) and Ni (III). Therefore, the use of a lower valency Ni (I)-species, such as nickel nitride, increases the amount of faradic charge in the redox reaction between Ni (I) and Ni (III), thereby increasing the specific capacitance of the material.

Secondly, while nickel nitride remains an attractive material for pseduocapacitive material development because of its two step oxidation/reduction reaction between Ni (I) and Ni (III), this material traditionally lacks the electron transport efficiency of nickel. In order to mitigate this issue, highly conductive graphene supports were employed by the authors.[19] Above all the tested carbon supports, rGO demonstrated to be the most promising material, due to its two-dimensional structure and high electrical conductivity, flexibility, mechanical strength, large specific surface area, and light weight.[135]

Graphene oxide was prepared according to the modified Hummer's method.[127] An amount of either aqueous or alcoholic GO was added to glycol to form a uniform brown-coloured suspension with high stirring and ultrasonication. Nickel nitrate hexahydrate was then dissolved in the suspension. Following the addition of 28wt%

ammonia dehydrate, the mixture underwent a 10 hour solvothermal treatment at 150 °C. The product was then washed and freeze dried. Finally, the sample was ramped at 5 °C/min to 350 °C and annealed for 2 hour under 20 sccm NH_3 flow.

Ni_3N-rGO composites were prepared using two different solution media: ethylene glycol and ethanol. The particles synthesized via a solvothermal method using ethylene glycol as solvent showed no XRD signals corresponding to NiO or $Ni(OH)_2$ after annealing with NH_3. The hexagonal closed pack phase of nickel nitride was confirmed by XRD with no peak interference from the rGO support, as 2-D morphology and poor crystallinity result in weak diffraction characteristics. TEM images of the Ni_3N showed small nanoparticles approximately 10 nm in size. The particles were visibly anchored to the underlying rGO supports, resulting in an excellent homogeneity and particle distribution as seen in Fig. 16.[19]

Ni_3N-rGO synthesized via a hydrothermal treatment in the presence of alcohol did not form phase pure nickel nitride. The nucleation and crystallization process of the nickel nitride occurred at a much slower rate, which resulted in the formation of thin layers of nickel hydroxide on the rGO support hydrate, as detected in XRD and TEM.

Based on Raman spectroscopy analysis, the Ni_3N-rGO composite material exhibited an increased intensity of the defect band (D-band), as compared to rGO support without particles. The increase in the D-band versus the graphitic band (G-band) can be attributed to the formation of the defects, due to nitrogen doping from the NH_3 treatment.[136]

The valence states of the Ni were explored with XPS. The Ni $2p_{3/2}$ showed a strong peak at 852.4 eV, which has been previously reported as the +1 state of Ni in the literature.[17, 46] Two distinct nitrogen species were identified in the N 1s spectrum. The peak at 397.4 eV derived from N^{-3} in Ni_3N.[17, 46] The other peak at 399.3 eV was characterized as a higher valent N species, resulting from nitrogen dopants in the rGO support.

The cyclability of the Ni_3N/rGO nanocomposite was tested using cyclic voltammetry with a Pt sheet and Ag/AgCl as counter and reference electrode, respectively. The cyclic voltammogram in Fig. 17 clearly shows the reversible conversion of Ni (I) -> Ni (II) -> Ni (III).[19] Even at larger scanning rates, the material maintained high specific capacitance (Cs) values above 750 Fg^{-1}, indicating that Ni (I) likely remains intact at least toward the more bulk regions of the sample despite the emergence of some Ni(II) species at 856.4 eV, evident in the high-resolution Ni 2p XPS spectra of the post-cycled sample.

This increased performance was only observed with the Ni_3N/rGO nanocomposite. Pure Ni_3N demonstrated poor pseudo-capacitance performance, with Cs values of no more than 100 Fg^{-1}. This highlights the importance of the flexile conductive substrate in improving the specific capacitance of the composite material. Moreover, the rGO support also played a major role in restricting the growth and size dispersion of the Ni_3N nanoparticles. As stated previously, the nanoparticle size of Ni_3N on rGO was approximately 10 nm, whereas the pure Ni_3N prepared with rGO ranged in size from 50-200 nm.
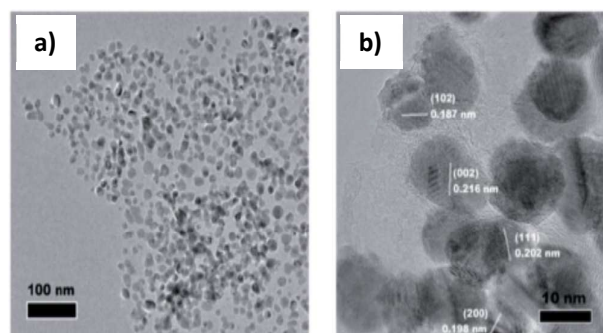

Fig. 16 (a) TEM and (b) HRTEM images of the Ni_3N/rGO nanocomposite. Reproduced from ref. 19. Copyright 2015 Royal Society of Chemistry
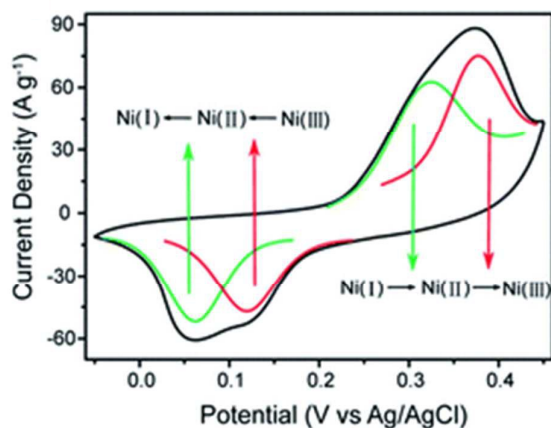
Fig. 17 CV curve of Ni$_3$N/rGO electrode at a scan rate of 20 mV s-1, with a Pt sheet and Ag/AgCl (in saturated KCl) as counter and reference electrodes, respectively, in 6 M KOH. Reproduced from Ref. 19. Copyright 2015, Royal Society of Chemistry

The smaller nanoparticle size also contributed to the performance of the pseudocapacitive material, as the small sized nanoparticles expose more surface to undergo faradic redox reaction. In addition, the volume change during faradic reaction is a significant factor for pseudocapacitive materials.[137] However, the flexibility of the rGO substrate and the strength of the Ni$_3$N particle adhesion to the substrate prevents structural breakdown.[138]

The durability of the nanocomposite was tested by cycling at different current densities. Even after 4000 cycles, the material maintained a specific capacity of more the 70 %. Even at the highest current density of 100 Ag^{-1}, the specific capacity was 791.7 Fg^{-1} after 4000 cycles.

The authors also fabricated an asymmetric supercapacitor cell to evaluate the material in practical supercapacitor applications. The asymmetric capacitors exhibited high specific capacitance at high current densities (2087.5 Fg^{-1} at 1 Ag^{-1} and 1160.8 Fg^{-1} at 100 Ag^{-1}). The device had a high energy density of 50.5 Whkg^{-1} at a power density of 800 Wkg^{-1} and exhibited a capacitance retention of 80 % after 500 cycles at different current densities.[19] With high specific capacitance and stability, the Ni$_3$N-rGO nanocomposites can be considered a viable candidate for nanostructured pseudo-supercapacitor electrode materials.

It is now clear that rGO supports impart the stability to nickel nitride catalysts, which traditionally lacked material robustness. In addition, it has also become apparent that rGO reduces the particle size significantly. It can by hypothesized that the porous nature of rGO provides abundant nucleation sites, whereon nickel nitride seeds can grow. Furthermore, the support seemingly anchors the nickel nitride particle; so that the migration of particles is limited and particle growth through Ostwald ripening is reduced.

Conclusions and Outlook

There is a growing interest in nickel nitride as a potential earth-abundant substitute to precious metal catalysts in a variety of catalytic reactions employed in energy-related applications.

Traditionally, the thermal instability of nickel nitride has limited its use in practical applications. However, this material is no longer merely a topic of academic study. Researchers have developed novel synthetic routes to synthesize nanostructured and porous nickel nitride materials, which possess the appropriate size and effective surface area to carry out catalytic reactions with meaningful efficiencies.

In addition, support materials have been deployed to add stability to this inherently unstable material. The fundamental studies conducted throughout the decades have given valuable insight into structure-property relationships. Knowing that nickel nitride is a poor conductor and inefficient electron transfer mediator, scientists have designed doped carbon support materials that not only impart stability, but also improve the electronic properties of nickel nitride. Therefore, through fundamental knowledge, the properties of nickel nitride nanocomposite materials can be synthetically tuned to further address specific catalytic needs.

Indeed, rational design of nickel nitride/ support nanocomposites is surely the way to further improve the performance and robustness of this material. Expanding from rGO supports, nickel nitride catalysts could be synthesized with mesoporous supports, which could further improve the structural integrity of nickel nitride and enhance the influence of the carbon support on the material properties. For example, integration of nickel nitride into doped mesoporous carbon could not only create nickel nitride nanoparticles with specific size and morphology, but also improve the thermal stability, chemical resistivity, and mechanical strength of nickel nitride catalysts.

Moreover, other support materials could be investigated, namely mesoporous silica. Both hard and soft-templating procedures could foster the development of supported-nickel nitride catalysts. A soft-templated, core-shell structure with a Ni$_3$N particle center and a mesoporous silica shell has been suggested. In addition, the incorporation of nickel nitride nanoparticles into the mesoporous silica structure through intercalation chemistry is an area of interest.

As demonstrated in this minireview, computational analysis can serve as a viable method to understand fundamental nickel nitride properties and help direct experimental design. Looking forward, computational efforts could be focused on comprehending the chemistry at the interface of the support material and catalyst. Through this, researchers could gain a better understanding of how the support materials affect catalytic properties.

This minireview outlines the advancement in nickel nitride synthesis and applications, summarizing current understanding of this material and providing a roadmap for future developments. The analysis of existing literature motivates the advancement of nanoscale supported and unsupported nickel nitride. However, the investigation of nickel nitride should go in tandem with the development of iron and cobalt carbide/nitride, as these materials do possess similar properties and synthetic challenges as nickel nitride.

Acknowledgements

References

1. R. B. Levy and M. Boudart, *Science*, 1973, **181**, 547-549.
2. A. S. Mamède, J. M. Giraudon, A. Löfberg, L. Leclercq and G. Leclercq, *Applied Catalysis A: General*, 2002, **227**, 73-82.
3. V. S. Palanker, R. A. Gajyev and D. V. Sokolsky, *Electrochimica Acta*, 1977, **22**, 133-136.
4. A. Alexander and J. Hargreaves, *Chemical Society Reviews*, 2010, **39**, 4388-4401.
5. C. Giordano, C. Erpen, W. Yao, B. Milke and M. Antonietti, *Chemistry of Materials*, 2009, **21**, 5136-5144.
6. E. Gregoryanz, C. Sanloup, M. Somayazulu, J. Badro, G. Fiquet, H. K. Mao and R. J. Hemley, *Nature materials*, 2004, **3**, 294-297.
7. C. Giordano and M. Antonietti, *Nano Today*, 2011, **6**, 366-380.
8. W. Chen, J. Muckerman and E. Fujita, *Chemical Communications*, 2013, **49**, 8896-8909.
9. X. Li and M. Antonietti, *Chemical Society Reviews*, 2013, **42**, 6593-6604.
10. W. Chen, K. Sasaki, C. Ma, A. Frenkel, N. Marinkovic, J. Muckerman, Y. Zhu and R. Adzic, *Angewandte Chemie-International Edition*, 2012, **51**, 6131-6135.
11. V. Molinari, C. Giordano, M. Antonietti and D. Esposito, *Journal of the American Chemical Society*, 2014, **136**, 1758-1761.
12. W. Yang, S. Rehman, X. Chu, Y. Hou and S. Gao, *ChemNanoMat*, 2015, **1**, 376-398.
13. D. C. Dunand and P. Müllner, *Advanced Materials*, 2011, **23**, 216-232.
14. C. H. Gong, Y. S. Jia, X. W. Zhao, H. J. Liu, X. Y. Lv, L. G. Yu, J. W. Zhang and J. F. Zhou, *Applied Physics Letters*, 2015, **107**, 153905.
15. Y. S. Jia, H. S. Pan, H. J. Meng, H. J. Liu, Z. Q. Wang, X. Li, L. L. Zhu, P. Chai and C. H. Gong, *Rsc Advances*, 2015, **5**, 14061-14064.
16. F. Gillot, J. Oro-Sole and M. Palacin, *Journal of Materials Chemistry*, 2011, **21**, 9997-10002.
17. Y. Wang, Z. Fu, X. Yue and Q. Qin, *Journal of the Electrochemical Society*, 2004, **151**, E162-E167.
18. X. J. Li, M. M. Hasan, A. L. Hector and J. R. Owen, *Journal of Materials Chemistry A*, 2013, **1**, 6441-6445.
19. Y. Yu, W. Y. Gao, Z. X. Shen, Q. Zheng, H. Wu, X. Wang, W. G. Song and K. J. Ding, *Journal of Materials Chemistry A*, 2015, **3**, 16633-16641.
20. S. H. Park, Y. H. Cho, M. Choi, H. Choi, J. S. Kang, J. H. Um, J. W. Choi, H. Choe and Y. E. Sung, *Surface & Coatings Technology*, 2014, **259**, 560-569.
21. J. Soo Kang, M.-A. Park, J.-Y. Kim, S. Ha Park, D. Young Chung, S.-H. Yu, J. Kim, J. Park, J.-W. Choi, K. Jae Lee, J. Jeong, M. Jae Ko, K.-S. Ahn and Y.-E. Sung, *Scientific Reports*, 2015, **5**, 10450.
22. Q. W. Jiang, G. R. Li, S. Liu and X. P. Gao, *The Journal of Physical Chemistry C*, 2010, **114**, 13397-13401.
23. C. H. Bartholomew and R. J. Farrauto, *Journal of Catalysis*, 1976, **45**, 41-53.
24. S. Ge and J. F. Hartwig, *Angewandte Chemie (International ed. in English)*, 2012, **51**, 12837-12841.
25. M. Stewart, M. Ho, S. Wiese, M. Lindstrom, C. Thogerson, S. Raugei, R. Bullock and M. Helm, *Journal of the American Chemical Society*, 2013, **135**, 6033-6046.
26. A. Alexander, J. Hargreaves and C. Mitchell, *Topics in Catalysis*, 2012, **55**, 1046-1053.
27. G. Clavel, V. Molinari, A. Kraupner and C. Giordano, *Chemistry-a European Journal*, 2014, **20**, 9018-9023.
28. M. Shalom, V. Molinari, D. Esposito, G. Clavel, D. Ressnig, C. Giordano and M. Antonietti, *Advanced Materials*, 2014, **26**, 1272-1276.
29. F. Alonso, P. Riente and M. Yus, *Accounts of Chemical Research*, 2011, **44**, 379-391.
30. K. Xu, P. Chen, X. Li, Y. Tong, H. Ding, X. Wu, W. Chu, Z. Peng, C. Wu and Y. Xie, *Journal of the American Chemical Society*, 2015, **137**, 4119-4125.
31. M. Shalom, D. Ressnig, X. Yang, G. Clavel, T. Fellinger and M. Antonietti, *Journal of Materials Chemistry a*, 2015, **3**, 8171-8177.
32. X. Huang, E. Zhu, Y. Chen, Y. Li, C.-Y. Chiu, Y. Xu, Z. Lin, X. Duan and Y. Huang, *Advanced Materials*, 2013, **25**, 2974-2979.
33. Y.-H. Chang, C.-T. Lin, T.-Y. Chen, C.-L. Hsu, Y.-H. Lee, W. Zhang, K.-H. Wei and L.-J. Li, *Advanced Materials*, 2013, **25**, 756-760.
34. R. Juza and W. Sachsze, *Zeitschrift für Anorganische Chemie*, 1943, **251**, 201-212.
35. R. Bernier, *Ann. Chim. Paris*, 1951, **6**, 104.
36. A. Baiker and M. Maciejewski, *Journal of the Chemical Society, Faraday Transactions 1: Physical Chemistry in Condensed Phases*, 1984, **80**, 2331-2341.
37. Y. Egashira and H. Komiyama, *Industrial & Engineering Chemistry Research*, 1990, **29**, 1583-1588.
38. R. S. Ningthoujam, N. S. Gajbhiye and S. Sharma, *Pramana-Journal of Physics*, 2009, **72**, 577-586.
39. F. Kahraman and S. Karadeniz, *Plasma Chemistry and Plasma Processing*, 2011, **31**, 595-604.
40. D. Vempaire, S. Miraglia, A. Sulpice, L. Ortega, E. Hlil, D. Fruchart and J. Pelletier, *Journal of Magnetism and Magnetic Materials*, 2004, **272**, E843-E844.
41. E. Lindahl, M. Ottosson and J. O. Carlsson, in *Eurocvd 17 / Cvd 17*, eds. M. T. Swihart, D. Barreca, R. A. Adomaitis and K. Worhoff, 2009, vol. 25, pp. 365-372.
42. E. Lindahl, M. Ottosson and J. O. Carlsson, *Surface & Coatings Technology*, 2010, **205**, 710-716.
43. E. Lindahl, M. Ottosson and J. O. Carlsson, *Journal of Vacuum Science & Technology A*, 2010, **28**, 1203-1209.
44. Z. Li, R. Gordon, V. Pallem, H. Li and D. Shenai, *Chemistry of Materials*, 2010, **22**, 3060-3066.
45. Z. Li, R. Gordon, H. Li, D. Shenai and C. Lavoie, *Journal of the Electrochemical Society*, 2010, **157**, H679-H683.
46. R. Dhunna, C. Lai, D. Avasthi, S. Barman, V. Ganesan and I. Jain, *Vacuum*, 2009, **83**, 1448-1453.
47. D. Vempaire, S. Miraglia, J. Pelletier, D. Fruchart, E. K. Hlil, L. Ortega, A. Sulpice and F. Fettar, *Journal of Alloys and Compounds*, 2009, **480**, 225-229.
48. D. Vempaire, F. Fettar, L. Ortega, F. Pierre, S. Miraglia, A. Sulpice, J. Pelletier, E. K. Hlil and D. Fruchart, *Journal of Applied Physics*, 2009, **106**, 073911.
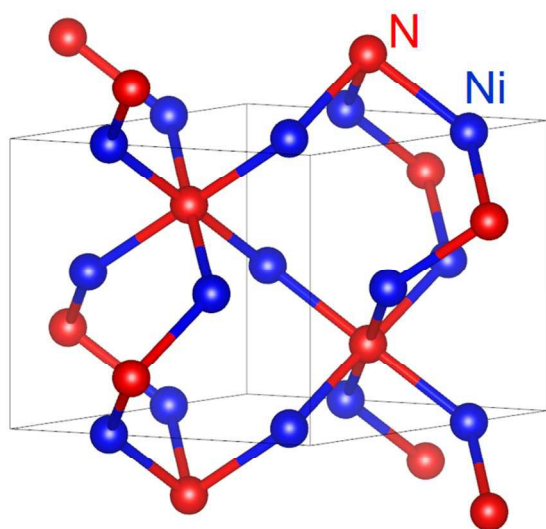
49. J. Choi and E. Gillan, *Inorganic Chemistry*, 2009, **48**, 4470-4477.

50. C. Guillaume, J. Morniroli, D. Frost and G. Serghiou, *Journal of Physics-Condensed Matter*, 2006, **18**, 8651-8660.

51. Z. Wang, W. Yu, J. Chen, M. Zhang, W. Li and K. Tao, *Journal of Alloys and Compounds*, 2008, **466**, 352-355.

52. B. Mazumder and A. Hector, *Topics in Catalysis*, 2009, **52**, 1472-1481.

53. A. Leineweber, H. Jacobs and S. Hull, *Inorganic Chemistry*, 2001, **40**, 5818-5822.

54. S. Desmoulins-Krawiec, C. Aymonier, A. Loppinet-Serani, F. Weill, S. Gorsse, J. Etourneau and F. Cansell, *Journal of Materials Chemistry*, 2004, **14**, 228-232.

55. N. Gajbhiye, R. Ningthoujam and J. Weissmuller, *Physica Status Solidi a-Applied Research*, 2002, **189**, 691-695.

56. R. S. Ningthoujam and N. S. Gajbhiye, *Indian Journal of Physics and Proceedings of the Indian Association for the Cultivation of Science-Part A*, 2004, **78A**, 265-269.

57. H. A. Wriedt, *Bulletin of Alloy Phase Diagrams*, **6**, 558-563.

58. A. Fernández Guillermet and K. Frisk, *International Journal of Thermophysics*, **12**, 417-431.

59. MTDATA, Calculated N-Ni phase diagram, (accessed March, 2016).

60. N. Brese and M. O'Keeffe, in *Complexes, Clusters and Crystal Chemistry*, Springer Berlin Heidelberg, 1992, vol. 79, ch. 6, pp. 307-378.

61. C. M. Fang, M. H. F. Sluiter, M. A. van Huis and H. W. Zandbergen, *Physical Review B*, 2012, **86**, 134114.

62. I. Neklyudov and A. Morozov, *Physica B-Condensed Matter*, 2004, **350**, 325-337.

63. A. Leineweber, H. Jacobs, W. Kockelmann, S. Hull and D. Hinz-Hübner, *Journal of Alloys and Compounds*, 2004, **384**, 1-5.

64. A. Leineweber, F. Lienert, S. L. Shang, Z. K. Liu and E. J. Mittemeijer, *Journal of Materials Research*, 2012, **27**, 1531-1541.

65. L. MAYA, *Journal of Vacuum Science & Technology a-Vacuum Surfaces and Films*, 1993, **11**, 604-608.

66. E. J. Mittemeijer and M. A. J. Somers, *Surface Engineering*, 1997, **13**, 483-497.

67. M. J. Somers and E. Mittemeijer, *MMTA*, 1995, **26**, 57-74.

68. T. G. Kollie, *Physical Review B*, 1977, **16**, 4872-4881.

69. J. M. D. Coey and P. A. I. Smith, *Journal of Magnetism and Magnetic Materials*, 1999, **200**, 405-424.

70. H. Pan, X. Cheng, C. Gong, L. Yu, J. Zhang and Z. Zhang, *Journal of Applied Physics*, 2013, **113**, 113906.

71. H. Pan, X. Cheng, C. Zhang, C. Gong, L. Yu, J. Zhang and Z. Zhang, *Applied Physics Letters*, 2013, **102**, 012410.

72. J. Zhang, C. Yan, S. Liu, H. Pan, C. Gong, L. Yu and Z. Zhang, *Applied Physics Letters*, 2012, **100**, 233104.

73. C.-M. Fang, R. S. Koster, W.-F. Li and M. A. van Huis, *RSC Advances*, 2014, **4**, 7885-7899.

74. S. Yan, L. Zhen, C. Xu, J. Jiang and W. Shao, *Journal of Physics D-Applied Physics*, 2010, **43**, 245003.

75. Z. Zetao, *J. Mater. Chem. C*, 2014, **2**, 6582-6591.

76. M. Raney, Method for producing Finely Divided Nickel, US Patent 1628190, Issued 1927-05-10.

77. H. Kobayashi, Y. Hosaka, K. Hara, B. Feng, Y. Hirosaki and A. Fukuoka, *Green Chemistry*, 2014, **16**, 637-644.

78. E. L. Smith, A. P. Abbott and K. S. Ryder, *Chemical Reviews*, 2014, **114**, 11060-11082.

79. P. Kuhn, A. Forget, J. Hartmann, A. Thomas and M. Antonietti, *Advanced Materials*, 2009, **21**, 897-901.

80. N. Fechler, T. Fellinger and M. Antonietti, *Advanced Materials*, 2013, **25**, 75-79.

81. P. Kuhn, M. Antonietti and A. Thomas, *Angewandte Chemie-International Edition*, 2008, **47**, 3450-3453.

82. J. Badding, *Advanced Materials*, 1997, **9**, 877-886.

83. K. Sakaushi and M. Antonietti, *Bulletin of the Chemical Society of Japan*, 2015, **88**, 386-398.

84. J. Zhu, K. Sakaushi, G. Clavel, M. Shalom, M. Antonietti and T. Fellinger, *Journal of the American Chemical Society*, 2015, **137**, 5480-5485.

85. E. A. Gelder, S. D. Jackson and C. M. Lok, *Chemical Communications*, 2005, 522-524.

86. Z. Sun, Y. Zhao, Y. Xie, R. Tao, H. Zhang, C. Huang and Z. Liu, *Green Chemistry*, 2010, **12**, 1007-1011.

87. C. Giordano and T. Corbiere, *Colloid and Polymer Science*, 2013, **291**, 1297-1311.

88. B. Cao, G. Veith, J. Neuefeind, R. Adzic and P. Khalifah, *Journal of the American Chemical Society*, 2013, **135**, 19186-19192.

89. K. Kuttiyiel, K. Sasaki, Y. Choi, D. Su, P. Liu and R. Adzic, *Nano Letters*, 2012, **12**, 6266-6271.

90. C. C. L. McCrory, S. Jung, J. C. Peters and T. F. Jaramillo, *Journal of the American Chemical Society*, 2013, **135**, 16977-16987.

91. N. H. Chou, P. N. Ross, A. T. Bell and T. D. Tilley, *ChemSusChem*, 2011, **4**, 1566-1569.

92. A. J. Esswein, Y. Surendranath, S. Y. Reece and D. G. Nocera, *Energy & Environmental Science*, 2011, **4**, 499-504.

93. M. Shalom, M. Guttentag, C. Fettkenhauer, S. Inal, D. Neher, A. Llobet and M. Antonietti, *Chemistry of Materials*, 2014, **26**, 5812-5818.

94. N. Danilovic, R. Subbaraman, D. Strmcnik, K.-C. Chang, A. P. Paulikas, V. R. Stamenkovic and N. M. Markovic, *Angewandte Chemie International Edition*, 2012, **51**, 12495-12498.

95. M. Biesinger, B. Payne, L. Lau, A. Gerson and R. Smart, *Surface and Interface Analysis*, 2009, **41**, 324-332.

96. J. Xie, J. Zhang, S. Li, F. Grote, X. Zhang, H. Zhang, R. Wang, Y. Lei, B. Pan and Y. Xie, *Journal of the American Chemical Society*, 2013, **135**, 17881-17888.

97. Y. Sun, Z. Sun, S. Gao, H. Cheng, Q. Liu, J. Piao, T. Yao, C. Wu, S. Hu, S. Wei and Y. Xie, *Nat Commun*, 2012, **3**, 1057.

98. Y. Sun, S. Gao, F. Lei and Y. Xie, *Chemical Society Reviews*, 2015, **44**, 623-636.

99. S. Ida, D. Shiga, M. Koinuma and Y. Matsumoto, *Journal of the American Chemical Society*, 2008, **130**, 14038-14039.

100. L. Trotochaud, J. K. Ranney, K. N. Williams and S. W. Boettcher, *Journal of the American Chemical Society*, 2012, **134**, 17253-17261.

101. Y. Yang, H. Fei, G. Ruan, C. Xiang and J. M. Tour, *ACS Nano*, 2014, **8**, 9518-9523.

102. R. D. L. Smith, M. S. Prévot, R. D. Fagan, Z. Zhang, P. A. Sedach, M. K. J. Siu, S. Trudel and C. P. Berlinguette, *Science*, 2013, **340**, 60-63.

103. L. Kuai, J. Geng, C. Chen, E. Kan, Y. Liu, Q. Wang and B. Geng, *Angewandte Chemie International Edition*, 2014, **53**, 7547-7551.

104. K. Fominykh, J. M. Feckl, J. Sicklinger, M. Döblinger, S. Böcklein, J. Ziegler, L. Peter, J. Rathousky, E.-W. Scheidt, T.

Bein and D. Fattakhova-Rohlfing, *Advanced Functional Materials*, 2014, **24**, 3123-3129.

105. M. Gao, W. Sheng, Z. Zhuang, Q. Fang, S. Gu, J. Jiang and Y. Yan, *Journal of the American Chemical Society*, 2014, **136**, 7077-7084.

106. L. Trotochaud, S. L. Young, J. K. Ranney and S. W. Boettcher, *Journal of the American Chemical Society*, 2014, **136**, 6744-6753.

107. M. Gong, Y. Li, H. Wang, Y. Liang, J. Z. Wu, J. Zhou, J. Wang, T. Regier, F. Wei and H. Dai, *Journal of the American Chemical Society*, 2013, **135**, 8452-8455.

108. S. Chen, J. Duan, M. Jaroniec and S. Z. Qiao, *Angewandte Chemie International Edition*, 2013, **52**, 13567-13570.

109. X. Long, J. Li, S. Xiao, K. Yan, Z. Wang, H. Chen and S. Yang, *Angewandte Chemie International Edition*, 2014, **53**, 7584-7588.

110. F. Song and X. Hu, *Nat Commun*, 2014, **5**, 4477.

111. Y. Lee, J. Suntivich, K. J. May, E. E. Perry and Y. Shao-Horn, *The Journal of Physical Chemistry Letters*, 2012, **3**, 399-404.

112. M. E. G. Lyons and S. Floquet, *Physical Chemistry Chemical Physics*, 2011, **13**, 5314-5335.

113. D. R. Dreyer, S. Park, C. W. Bielawski and R. S. Ruoff, *Chemical Society Reviews*, 2010, **39**, 228-240.

114. D. Chen, L. Tang and J. Li, *Chemical Society Reviews*, 2010, **39**, 3157-3180.

115. Y. Zhong, X. Wang, K. Jiang, J. Y. Zheng, Y. Guo, Y. Ma and J. Yao, *Journal of Materials Chemistry*, 2011, **21**, 17998-18002.

116. X. Zhu, Y. Zhu, S. Murali, M. D. Stoller and R. S. Ruoff, *ACS Nano*, 2011, **5**, 3333-3338.

117. L. F. Lai, J. X. Zhu, B. S. Li, Y. D. Zhen, Z. X. Shen, Q. Y. Yan and J. Y. Lin, *Electrochimica Acta*, 2014, **134**, 28-34.

118. I. Alphonsa, A. Chainani, P. M. Raole, B. Ganguli and P. I. John, *Surface and Coatings Technology*, 2002, **150**, 263-268.

119. R. Franke, *Spectrochimica Acta Part A: Molecular and Biomolecular Spectroscopy*, 1997, **53**, 933-941.

120. S. Komaba, W. Murata, T. Ishikawa, N. Yabuuchi, T. Ozeki, T. Nakayama, A. Ogata, K. Gotoh and K. Fujiwara, *Advanced Functional Materials*, 2011, **21**, 3859-3867.

121. P. Ge and M. Fouletier, *Solid State Ionics*, 1988, **28**, 1172-1175.

122. V. Vallet, U. Wahlgren and I. Grenthe, *Journal of the American Chemical Society*, 2003, **125**, 14941-14950.

123. D. V. Baxter, M. H. Chisholm, G. J. Gama, V. F. DiStasi, A. L. Hector and I. P. Parkin, *Chemistry of Materials*, 1996, **8**, 1222-1228.

124. in *Infrared and Raman Spectroscopy*, Wiley-VCH Verlag GmbH, 1995, pp. 711-764.

125. C. Vidal-Abarca, P. Lavela, J. L. Tirado, A. V. Chadwick, M. Alfredsson and E. Kelder, *Journal of Power Sources*, 2012, **197**, 314-318.

126. W. S. Hummers and R. E. Offeman, *Journal of the American Chemical Society*, 1958, **80**, 1339-1339.

127. D. C. Marcano, D. V. Kosynkin, J. M. Berlin, A. Sinitskii, Z. Sun, A. Slesarev, L. B. Alemany, W. Lu and J. M. Tour, *ACS Nano*, 2010, **4**, 4806-4814.

128. Z.-W. Fu, Y. Wang, X.-L. Yue, S.-L. Zhao and Q.-Z. Qin, *The Journal of Physical Chemistry B*, 2004, **108**, 2236-2244.

129. M. P. Yeager, D. Su, N. S. Marinković and X. Teng, *Journal of The Electrochemical Society*, 2012, **159**, A1598-A1603.

130. D. Su, H.-S. Kim, W.-S. Kim and G. Wang, *Chemistry – A European Journal*, 2012, **18**, 8224-8229.

131. X. Zhang, W. Shi, J. Zhu, W. Zhao, J. Ma, S. Mhaisalkar, T. Maria, Y. Yang, H. Zhang, H. Hng and Q. Yan, *Nano Res.*, 2010, **3**, 643-652.

132. C. Yuan, X. Zhang, L. Su, B. Gao and L. Shen, *Journal of Materials Chemistry*, 2009, **19**, 5772-5777.

133. J. Y. Lee, K. Liang, K. H. An and Y. H. Lee, *Synthetic Metals*, 2005, **150**, 153-157.

134. B. Zhao, J. Song, P. Liu, W. Xu, T. Fang, Z. Jiao, H. Zhang and Y. Jiang, *Journal of Materials Chemistry*, 2011, **21**, 18792-18798.

135. K. S. Novoselov, A. K. Geim, S. V. Morozov, D. Jiang, Y. Zhang, S. V. Dubonos, I. V. Grigorieva and A. A. Firsov, *Science*, 2004, **306**, 666-669.

136. C. Zhang, L. Fu, N. Liu, M. Liu, Y. Wang and Z. Liu, *Advanced Materials*, 2011, **23**, 1020-1024.

137. X. Lu, G. Wang, T. Zhai, M. Yu, S. Xie, Y. Ling, C. Liang, Y. Tong and Y. Li, *Nano Letters*, 2012, **12**, 5376-5381.

138. X. Lu, T. Liu, T. Zhai, G. Wang, M. Yu, S. Xie, Y. Ling, C. Liang, Y. Tong and Y. Li, *Advanced Energy Materials*, 2014, **4**, 1301944.

This minireview discusses controlled chemical synthetic advancements of nickel nitride and its composites, their fundamental properties, and energy-related applications.

338x190mm (96 x 96 DPI)